

Article

High Sulfur in Primitive Arc Magmas, Its Origin and Implications

Michael Zelenski ^{1,*} , Vadim S. Kamenetsky ^{1,2} , Nikolai Nekrylov ¹  and Alkiviadis Kontonikas-Charos ³

¹ Institute of Experimental Mineralogy RAS, 142432 Chernogolovka, Russia; dima.kamenetsky@utas.edu.au (V.S.K.); nekrilov.n@gmail.com (N.N.)

² Institute of Volcanology and Seismology, FEB RAS, 683006 Petropavlovsk-Kamchatsky, Russia

³ Helmholtz-Zentrum Dresden-Rossendorf, Helmholtz Institute Freiberg for Resource Technology, 09599 Freiberg, Germany; a.kontonikas-charos@hzdr.de

* Correspondence: volcangas@gmail.com

Abstract: Sulfur contents in 98.5% of melt inclusions (MI) from calc-alkaline subduction basalts do not exceed 4000 ppm, whereas experimentally established limits of sulfur solubility in basaltic melts with high fO_2 (characteristic of subduction zones, e.g., QFM + 2) surpass 14,000 ppm. Here we show that primitive (Mg# 62–64) subduction melts may contain high sulfur, approaching the experimental limit of sulfur solubility. Up to 11,700 ppm S was measured in olivine-hosted MI from primitive arc basalt from the 1941 eruption of the Tolbachik volcano, Kamchatka. These MI often contain magmatic sulfide globules (occasionally enriched in Cu, Ni, and platinum-group elements) and anhydrite enclosed within a brown, oxidized glass. We conclude that the ubiquitous low sulfur contents in MI may originate either from insufficient availability of sulfur in the magma generation zone or early magma degassing prior to inclusion entrapment. Our findings extend the measured range of sulfur concentrations in primitive calc-alkaline basaltic melts and demonstrate that no fundamental limit of 4000 ppm S exists for relatively oxidized subduction basalts, where the maximum sulfur content may approach the solubility limit determined by crystallization of magmatic anhydrite.

Keywords: melt inclusion; primitive arc basalt; high sulfur; magmatic anhydrite



check for updates

Citation: Zelenski, M.; Kamenetsky, V.S.; Nekrylov, N.; Kontonikas-Charos, A. High Sulfur in Primitive Arc Magmas, Its Origin and Implications. *Minerals* **2022**, *12*, 37. <https://doi.org/10.3390/min12010037>

Academic Editors: Magdalena Dumańska-Słowik, Beata Naglik, Tomasz Toboła and Giovanni Ruggieri

Received: 16 November 2021

Accepted: 21 December 2021

Published: 26 December 2021

Publisher's Note: MDPI stays neutral with regard to jurisdictional claims in published maps and institutional affiliations.



Copyright: © 2021 by the authors. Licensee MDPI, Basel, Switzerland. This article is an open access article distributed under the terms and conditions of the Creative Commons Attribution (CC BY) license (<https://creativecommons.org/licenses/by/4.0/>).

1. Introduction

The behavior of sulfur in magmatic systems is complex and not fully understood due to the fact that sulfur has several valence states from -2 to $+6$ and may form solid, liquid, or gaseous compounds, which are simultaneously present in magma. Spectroscopic methods show that silicate melt may contain sulfate (S^{6+}), sulfide (S^{2-}), or both sulfur species [1]. According to the experimental data, sulfur concentration in silicate melts is limited by the exsolution of a sulfur-containing phase. Depending on fO_2 , external pressure, and melt composition, this phase may be either a sulfide melt, a sulfate phase (in most cases, crystals of magmatic anhydrite ($CaSO_4$)), or solid sulfides (pyrrhotite) in the case of a relatively low-temperature silica-rich melt [2].

The solubility of sulfide in silicate melt controls the separation of sulfide liquid and, hence, the formation of magmatic sulfide deposits [3,4], whereas the solubility of sulfate is critical for assessing the extent of sulfur degassing during volcanic eruptions, e.g., [5]. For more than half a century, empirical, semi-empirical, and thermodynamic models have attempted to estimate the solubility of sulfide and sulfate in magma [2] based on melt composition, fO_2 , temperature, pressure, the presence of an aqueous fluid, and other parameters, e.g., [5–9]. The sulfur content in silicate melt in equilibrium with sulfide melt (SCSS, sulfur content at sulfide saturation) typically does not exceed 1300 ppm S in a reducing environment ($fO_2 \leq$ QFM [3], and references therein). With an increase in oxygen fugacity, the solubility of sulfur in the silicate melt increases, and at $fO_2 \sim$ QFM + 1 . . . 2 is determined by equilibrium with magmatic anhydrite (SCAS, sulfur content at anhydrite

saturation), reaching at most 14,000 ppm S for dry basaltic melts at 1 GPa [3,4]. This oxygen fugacity is not fixed and depends on the silicate melt composition and, to a lesser extent, pressure, e.g., [2], and references therein, [10,11]. The situation is even more complicated in the presence of a fluid phase in which sulfur is present predominantly in the form of H₂S (S²⁻) and SO₂ (S⁴⁺), and where sulfur is redistributed in accordance with the equilibrium partition coefficients in the melt-fluid system. These coefficients largely depend on pressure, e.g., [12], *f*O₂, and FeO content [13], and the degree of the melt polymerization [2].

In the meantime, concentrations of volatile components in magmas, including sulfur, are primarily obtained from studies of melt inclusions (MI) [14]. High sulfur concentrations measured experimentally in basaltic melts (~14,000 ppm S [3]) have not yet been observed in natural calc-alkaline basalts. The maximum sulfur in island arc melts (excluding exotic alkaline rocks such as basanite, leucite basanite, and minette [15,16]) was measured in melt inclusions at approximately 6000 ppm S, e.g., [17,18], with 99% of measurements being below 4300 ppm S (98.5% below 4000 ppm S), and a mean of only 1030 ppm. In most cases, the low sulfur content in MI does not reflect initial concentrations in the melt, as sulfur may have degassed before entrapment or could have fractionated into shrinkage bubbles within the inclusions [19]. It is unclear why the upper limit in S-rich MI is approximately 4000 ppm. Currently, no fundamental physicochemical factors are known that could limit sulfur solubility in silicate melt below SCSS or SCAS in the presence of a sulfide/sulfate phase, respectively. Therefore, low sulfur concentrations in natural MI may simply reflect the initially low sulfur availability in the slab fluid, slab melt, or mantle wedge in the magma generation zone.

Here we present new data from naturally occurring S-rich melt inclusions from primitive arc basalts in an attempt to resolve the apparent contradiction between high sulfur in experimental basaltic melts, much lower sulfur concentrations in natural melt inclusions, and the possible fractionation of sulfur into shrinkage bubbles within inclusions. According to these data, up to 11,700 ppm S was measured in MI in olivine crystals from the 1941 Tolbachik eruption. Such a high concentration is more than twice the previously measured concentrations of sulfur in primitive arc basalts and is close to the limiting value of sulfur solubility in oxidized basaltic melts as determined experimentally.

2. Sampling and Methods

Samples of basaltic scoria and ablated olivine crystals (remnants of melt were blown away) were collected from the foot of the 1941 eruptive cone of the Plosky Tolbachik volcano, Kamchatka (55.790° N, 160.336° E, Supplementary Figures S1 and S2). Similarly, olivine-bearing tephra was sampled at the foot of the eruptive cone during the Tolbachik eruption in July 2013 (55.765° N, 160.318° E). In the laboratory, scoria was crushed, and the heavy fraction containing olivine was separated in a heavy liquid with a density of 2.97 (tetrabromoethane). Olivine crystals 0.5–3 mm in size, containing large (>50 μm) naturally quenched melt inclusions, were manually picked under a stereomicroscope. Inclusions were exposed at the surface and polished using 1 μm diamond powder. Preliminary assessment of concentrations of rock-forming elements, sulfur, and chlorine in MI was performed using an electron microscope with an energy-dispersive spectrometer (Vega Tescan II XMU, Institute of Experimental Mineralogy, Chernogolovka). The following operating conditions were used: accelerating voltage of 20 kV, beam current of 0.3 nA, and counting time of 100 s. Quantitative analysis of MI compositions were performed on a Cameca SX100 electron microprobe (Vernadsky Institute of Geochemistry and Analytical Chemistry of Russian Academy of Sciences, Moscow). Analytical conditions were 15 kV accelerating voltage, 40 nA probe current, 10 μm defocused spot, and counting times of 20 s for major elements and 100 s for sulfur and chlorine; matrix effects were corrected using the ZAF method. The calibration standards were quartz (Si), rutile (Ti), San Carlos olivine (Mg, Fe), albite (Na, Al), CaWO₄ (Ca), orthoclase (K), MnO (Mn), BaSO₄ (S), and scapolite (Cl). Whole-rock major and trace elements were determined by XRF and ICP-MS in the Geoscience Laboratories, Sudbury, Ontario. The volatile contents (H₂O, CO₂, F, S, and Cl)

and isotopic composition of sulfur ($\delta^{34}\text{S}$) in selected melt inclusions were measured on a Secondary Ion Mass Spectrometer (SIMS) CAMECA IMS 1280 HR2 (Centre de Recherches Pétrographiques et Géochimiques, Nancy, France) following the technique described by Hauri et al. [20] and Gurenko et al. [21]. Only the inclusions from the 1941 Tolbachik eruption were studied by SIMS, the inclusions from the 2013 eruption were analyzed using EMPA (CAMECA SX100 electron microprobe, Vernadsky Institute of Geochemistry and Analytical Chemistry RAS, Moscow, Russia) Details of the analytical methods used for the ion microprobe volatile and isotopic measurements can be found in Gurenko et al. [21], Kamenetsky et al. [22], and Gurenko [23]. The SIMS method is considered one of the most up-to-date and accurate methods for measuring concentrations of volatile components (H_2O , CO_2 , F, S, and Cl) in glasses, but requires the most expensive equipment.

3. Results

3.1. Rocks and Melt Inclusions of Tolbachik

Scoria from the 1941 eruption of Tolbachik volcano, Kamchatka, contains 50.5–51.0 wt.% SiO_2 , 8.7–8.9 wt.% MgO , and 1.3–1.4 wt.% K_2O (Supplementary Table S1). The Mg# reaches 62–64, i.e., it can be characterized as primitive high-K magnesian basalt. The rock contains 3%–4% olivine phenocrysts with normal zonation (Figure 1A) and Mg# ranging from 85 to 92. Olivine crystals are typically 1–3 mm in size but can be up to 8 mm. Rare crystals of chromium spinel (Cr# ~ 65–75, Mg# ~ 58–63), up to 3 mm in size, are also present. Crystals of pyroxene are rare. The groundmass contains smaller crystals of olivine, clinopyroxene, plagioclase, Ti-magnetite, and glass. See Kamenetsky et al. [22] for further details on rock and phenocrysts compositions. Concentrations of all rock-forming and trace elements in basalt from the 1941 Tolbachik eruption are given in Supplementary Table S1.

Naturally quenched MI occurs exclusively in scoria or ablated olivine crystals (Figure 1), whereas lavas only contain crystallized MI. Inclusions from scoria contain either transparent glass (Figure 1B) or a fine crystalline aggregate composed of μm -sized crystallites (Figure 1C). Quenched MI from Tolbachik containing the fine crystalline aggregate differs from slowly cooled inclusions in which sizes of daughter crystals are comparable to the size of the inclusion (Supplementary Figure S3). Glass in the quenched inclusions ranges from light yellow, almost colorless and transparent (Figure 1B, Supplementary Figure S4), to translucent dark brown (Figure 1C, inclusions # 2–3, Supplementary Figures S5 and S6) or opaque dark gray. The latter is due to the presence of sub μm -sized crystals of clinopyroxene, anhydrite, and magnetite. Olivine crystals may contain both transparent (glassy) and opaque (finely crystallized) inclusions (Figure 1C). As the quenching rate is the same for adjacent inclusions, this difference in appearance likely reflects varying compositions of the inclusions. Analyses indicate systematically higher volatile contents (H_2O , F, S, and Cl) in finely crystallized inclusions. The difference in appearance between glassy and crystallized melt inclusions located in the same crystal can be explained by the fact that high volatile content in a silicate melt promotes a high nucleation rate of crystal nuclei, e.g., [24] and faster crystal growth due to a decrease in the viscosity of the melt, e.g., [25,26]. This is why less viscous basaltic melt containing a lot of water crystallizes faster and does not form glass upon quenching, e.g., [27], despite the lower crystallization temperature of water-saturated silicate melts. The works cited above consider the influence of water in the melt on the nucleation rate and crystal growth; however, according to our observations, sulfur can cause the same effect.

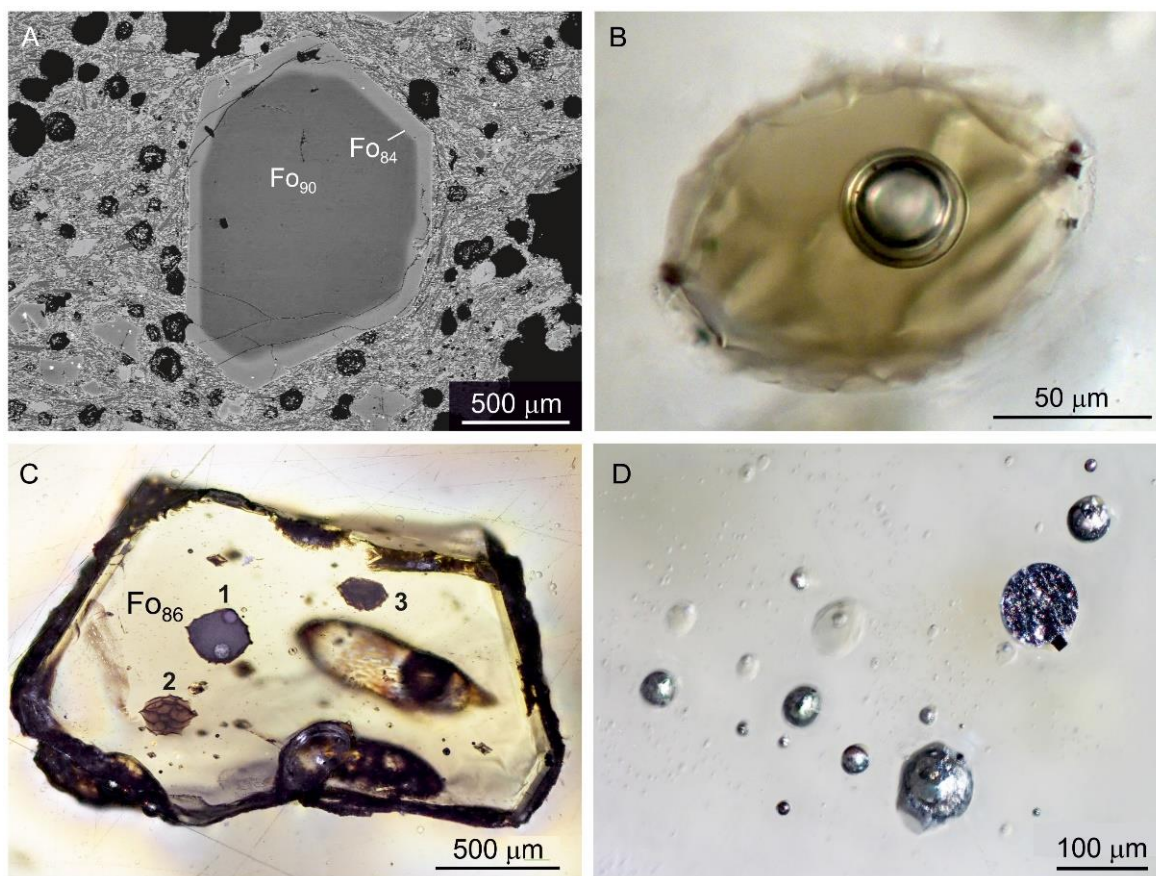


Figure 1. Back-scattered electron (A) and transmitted light (B–D) images of Tolbachik high-Mg basalts and melt inclusions. (A) The texture of the 1941 Tolbachik basalt, comprising large, normally zoned olivine phenocrysts (center) surrounded by a porous groundmass. (B) Large, 150- μm sized glassy melt inclusion with a shrinkage bubble partially filled with H_2O -rich fluid. (C) Olivine crystal with several glassy and crystallized melt inclusions, containing high sulfur: 1–0.91 wt.% S, the inclusion is opaque and contains fine crystallites of clinopyroxene and anhydrite; 2 and 3—glassy (translucent) melt inclusions with 0.51–0.61 wt.% S. See Figure 5 for more detail; the different appearance of MI in a single olivine crystal is explained below. (D) A swarm of sulfide inclusions in an olivine crystal. In addition to sulfides, the crystal contains glassy melt inclusions, but without sulfide globules. One of the sulfide globules is exposed on the polished surface.

The composition of the glass (or the fine-crystalline aggregate) in the inclusions corresponds to basaltic melt, which is close to the bulk composition of lavas from the 1941 Tolbachik eruption (Table 1, Supplementary Table S1). The average content of MgO and FeO in inclusions (7.73 wt.% on a volatile-free basis) is slightly lower than those in lavas (8.8 wt.%), which can be explained by olivine crystallization on the inclusion walls. We did not perform correction of melt inclusions for in-situ olivine crystallization in order to preserve the compatibility with the large data set from the GEOROC database where mostly raw data (without on-wall correction) are published. A detailed description of the composition of MI from the 1941 Tolbachik eruption, including those corrected for olivine crystallization on the inclusion walls, is given in Kamenetsky et al. [22]. According to these authors, the compositions of MI after correction correspond to much more primitive melts than the bulk composition of lavas of the 1941 Tolbachik eruption. For uncorrected compositions of the inclusions in the study, variations of metal contents are observed within a wide range (data below is given for the most common compositions, with 5% of extremely high and low values being truncated): Na_2O —1.43%–3.34%, MgO—3.65%–9.07%, Al_2O_3 —12.33%–16.88%, K_2O —0.54%–1.65%, CaO—9.93%–15.91%, Fe as total FeO—6.45%–10.48%, and SiO_2 —45.09%–52.55%. Such variability in MI compositions can be caused by the mixing

between magma of different compositions, the evolution of magma, and the assimilation of crustal material [22].

Table 1. Chemical composition of olivine-hosted melt inclusions, wt. %.

Sample	SiO ₂ wt. %	TiO ₂ wt. %	Al ₂ O ₃ wt. %	MgO wt. %	CaO wt. %	FeO wt. %	MnO wt. %	Na ₂ O wt. %	K ₂ O wt. %	P ₂ O ₅ wt. %	Total oxides	H ₂ O wt. %	CO ₂ ppm	F, ppm	S, ppm	Cl, ppm	δ ³⁴ S, ‰	Total wt. %
M-2-1	47.24	1.49	12.53	6.77	12.52	11.08	0.29	1.60	0.19	0.26	93.97	3.59	<dl	813	10523	227	n/m	98.71
M-3-1	47.16	1.32	11.94	7.38	11.63	9.20	0.38	2.59	0.86	0.35	92.81	4.53	2212	429	10322	945	6.5	98.73
M-3-2	46.93	1.35	11.92	7.52	12.33	9.37	0.18	2.35	0.87	0.20	93.03	4.46	1836	429	9829	1368	5.8	98.83
M-4-1	48.25	1.44	16.31	2.46	14.40	7.00	0.13	3.33	0.85	0.22	94.39	2.85	<dl	805	9742	1591	2.9	98.45
M-6-1	47.23	0.94	12.89	8.04	11.94	8.52	0.11	2.60	0.71	0.63	93.62	4.19	2394	493	9427	1376	3.5	99.17
M-6-2	50.70	1.30	16.37	5.45	11.05	8.48	0.08	3.69	1.35	0.05	98.50	1.00	128	449	545	751	3.4	99.70
M-7-1	49.12	0.94	13.68	6.22	12.26	8.08	0.23	3.19	0.93	0.13	94.77	2.49	<dl	870	5826	1294	n/m	98.06
M-8-1	45.47	1.68	14.04	8.36	11.50	8.96	0.29	3.21	0.82	0.46	94.78	3.87	<dl	602	4864	907	5.2	99.29
M-8-2	45.02	1.95	14.31	7.99	11.80	9.34	<dl	2.82	0.95	0.22	94.41	4.18	5307	472	3538	1305	5.7	99.66
M-9-1	47.72	1.22	14.91	7.35	11.62	7.56	0.17	3.66	1.25	0.22	95.68	3.16	5961	580	2837	1185	3.6	99.90
M-9-2	47.12	1.03	14.12	8.03	11.99	7.98	0.11	3.09	0.68	0.15	94.31	4.16	2769	497	3661	1454	4.2	99.30
M-10-1	53.40	0.50	10.31	8.73	13.24	7.63	0.14	1.09	0.21	0.15	95.40	3.59	799	406	3134	271	4.5	99.46
M-12-1	48.49	1.05	13.28	8.49	11.09	8.09	0.09	2.83	0.57	0.20	94.17	4.65	2376	510	3131	1376	4.9	99.56
M-12-2	49.31	0.72	13.21	8.72	11.02	8.10	0.10	3.14	0.75	0.39	95.46	3.92	2288	470	3084	1293	6	100.09
M-13-1	48.39	1.17	13.87	6.33	12.44	7.70	0.04	3.06	0.97	0.11	94.08	4.65	2663	482	3186	1367	4.9	99.50
M-13-2	45.76	1.21	15.85	7.26	13.31	6.81	0.17	3.33	0.99	0.11	94.81	3.89	2365	542	3322	1423	n/m	99.46
M-14-1	41.57	2.59	13.93	8.22	12.40	9.86	0.24	2.59	0.90	0.84	93.13	5.43	3865	600	3656	1130	4	99.48
N-1-1	45.69	1.02	13.99	8.76	10.23	9.16	n/m	2.90	0.67	0.21	92.63	4.76	2702	488	6412	1225	7.3	98.47
N-2-1	49.83	0.97	13.87	5.79	12.03	6.22	n/m	2.73	0.77	0.35	92.55	5.28	3673	596	8707	1525	4.8	99.27
N-2-2	46.72	1.47	12.94	7.14	11.44	9.71	n/m	2.07	0.31	0.31	92.12	4.55	<dl	521	7502	1447	5	97.62
N-3-1	50.72	0.96	14.24	5.72	12.42	6.85	n/m	2.81	0.80	0.53	95.05	3.26	1135	513	9756	1478	3.5	99.60
N-4-1	47.45	0.79	12.92	8.31	11.84	8.55	n/m	2.16	0.68	0.24	92.93	4.47	2663	515	7906	1270	3.6	98.64
N-4-2	47.06	1.11	14.41	6.69	12.42	7.30	n/m	3.14	0.88	0.50	93.51	4.37	2223	521	3040	1356	3.1	98.60
N-4-3	48.17	1.26	14.05	5.66	13.44	7.81	n/m	2.48	0.80	0.17	93.84	3.58	2065	584	4116	1452	4.9	98.24
N-5-1	46.14	1.58	15.33	8.11	9.84	9.81	n/m	2.89	0.54	0.29	94.53	5.00	2022	537	4242	1520	5.1	100.36
N-5-2	45.80	0.96	14.56	8.83	9.49	9.11	n/m	2.09	0.60	0.41	91.85	4.99	3348	568	5006	1261	4.4	97.85
N-6-1	48.38	1.28	15.62	7.57	9.84	9.17	n/m	3.38	0.95	0.00	96.18	2.85	3810	470	1990	877	5	99.74
N-8-1	52.26	0.64	13.43	7.36	11.68	7.05	n/m	1.74	0.61	0.57	95.35	2.71	<dl	694	11,675	963	5.1	99.39
N-9-1	47.63	0.77	14.85	6.49	12.11	8.17	n/m	2.33	0.64	0.09	93.08	4.03	2774	566	3230	1383	5.6	97.90
N-9-2	46.70	1.12	17.10	4.48	13.93	7.09	n/m	2.78	0.78	0.19	94.17	3.89	2166	567	3488	1376	4.4	98.82
N-10-1	47.95	0.99	13.92	7.19	11.49	8.08	n/m	3.12	0.86	0.25	93.85	3.54	5647	584	3006	1078	4.7	98.43
N-11-1	48.14	0.65	13.15	8.74	11.57	7.74	n/m	2.73	0.72	0.19	93.63	3.13	1451	542	2326	1026	3.4	97.29
N-12-1	47.18	0.89	13.94	8.00	11.27	7.46	n/m	2.95	0.94	0.56	93.18	3.96	3406	501	2952	1229	5.9	97.96
N-12-1	45.63	0.91	13.87	8.89	11.93	7.81	n/m	1.92	0.72	0.63	92.32	4.08	2805	503	2955	1249	6.5	97.15
N-13-1	46.66	1.77	13.33	8.00	12.21	7.99	n/m	1.85	0.81	0.52	93.14	4.41	2000	604	9251	843	1.6	98.83
N-14-1	47.39	0.97	13.96	7.63	14.16	6.63	n/m	2.66	0.82	0.44	94.68	3.56	2544	541	2998	1329	5.7	98.98
N-15-1	47.07	0.65	13.47	8.76	11.34	7.74	n/m	2.79	0.41	0.00	92.23	4.33	3211	464	2985	1182	5.6	97.35
N-16-1	46.74	0.83	16.08	4.43	14.36	7.75	n/m	2.35	0.47	0.30	93.30	3.84	7592	409	2044	1097	3.4	98.26

Supplementary Table S1 also contains data for MI from the 2013 Tolbachik eruption. These data are not discussed in detail because they are represented by inclusions that have undergone a significant degree of degassing. The data are used only for comparison of sulfur and chlorine contents in Figure 2 to demonstrate that MI in olivines from the 1941 Tolbachik eruption contain much more sulfur (there was virtually no degassing before the 1941 inclusions were entrapped).

3.2. Volatile Components in Melt Inclusions

Volatiles in the inclusions were measured by Electron Microprobe Analysis (EMPA) and Secondary Ion Mass Spectrometry (SIMS) methods. EMPA provides data for F, S, and Cl with a typical accuracy of around ± 100 ppm. Table 1 shows concentrations of volatiles (measured by SIMS) and rock-forming oxides (measured by EDS) for 38 melt inclusions. Additional information on sulfur, chlorine, and rock-forming oxides concentrations from another 343 melt inclusions from the 1941 and 2013 Tolbachik eruptions, and 25 measurements of matrix glass from the 1941 Tolbachik eruption are provided in Supplementary Table S2.

Aside from sulfur, concentrations of volatile elements (Table 1) are characteristic of melt inclusions in olivine from subduction volcanoes: H₂O up to 5.43%, CO₂ up to 7600 ppm, F up to 870 ppm, and Cl up to 1600 ppm. Sulfur concentrations obtained via SIMS are approximately in the same range as those measured by EMPA or EDS (545–11700 ppm). No significant correlations between volatiles are observed, except from that between S and Cl which is likely related to the degassing trend (Figure 2). For comparison, melt inclusions from the 2013 Tolbachik eruption and compositions of groundmass glass from basaltic scoria are also shown.

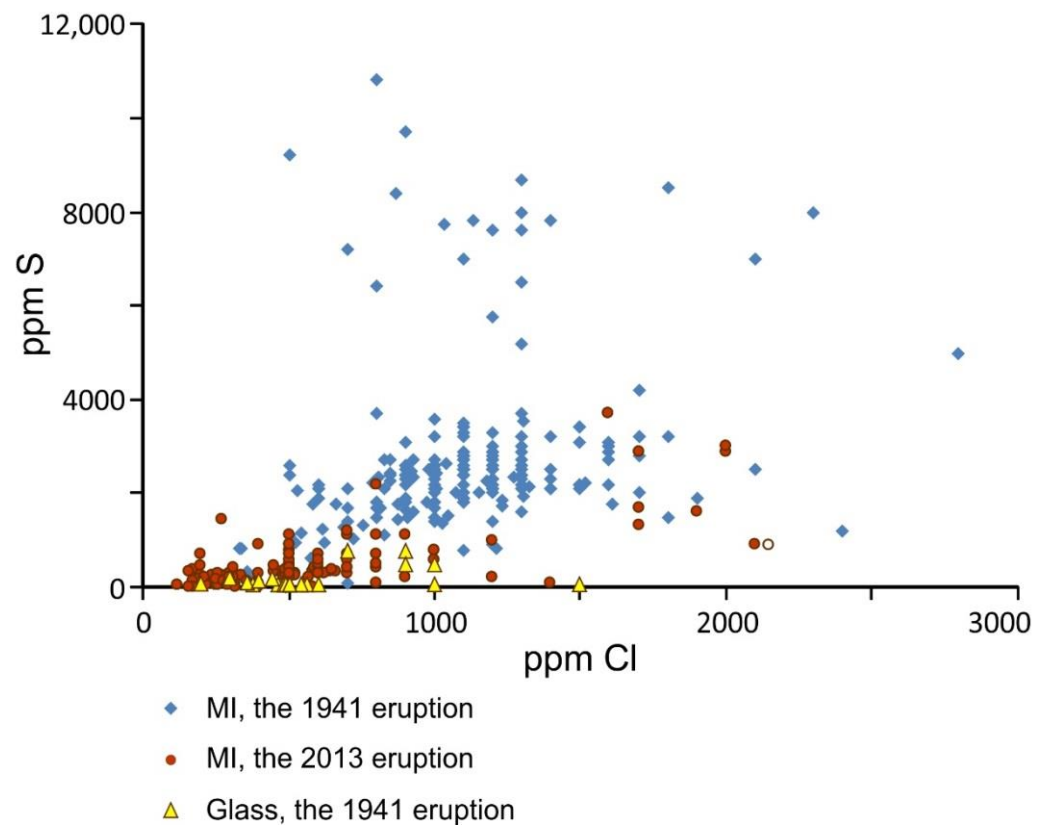


Figure 2. Variation diagram for Cl vs. S for naturally quenched melt inclusions from the 1941 and 2012–13 Tolbachik eruptions and groundmass glass for comparison. About 90% of inclusions fall on the degassing trend. The minimum sulfur concentration in quenched glasses is 50–60 ppm with chlorine equal to 300–500 ppm. The maximum sulfur concentrations in common non-degassed MI from the 1941 Tolbachik eruption reach 3200–3600 ppm S with chlorine of up to 1500 ppm. Melt inclusions in olivine from the 2013 Tolbachik eruption are shown for comparison. The 2013 inclusions represent high-alumina basalts (Supplementary Table S2) and form a similar degassing trend, but with systematically lower sulfur and chlorine concentrations. Modified from [28]; new data added.

Some inclusions (~2–3%) do not follow the typical degassing trend and record increased sulfur concentrations ranging from 4000–11700 ppm. Such inclusions tend to have darker (brown or dark gray) colors (Figure 1C and Figure 5, Supplementary Figures S5 and S6) and are often represented by a fine crystalline aggregate rather than glass (Figure 5B). This fine-crystalline aggregate crystallized inside the inclusion, and thus, the average composition of the inclusion should accurately reflect the composition of the melt. In order to avoid analytical errors caused by possible non-uniform distribution of the analyzed substances (e.g., sulfur), multiple spots (typically, 3–5) were placed during the volatile component analyzes. The deviation from the mean over three points for most inclusions was no more than 3.5% and for some inclusions, it was less than 1%, including high-sulfur ones (9755 ppm S, inclusion N-3-1). Such small deviations indicate a high degree of sulfur homogeneity in the melt. Only several inclusions had a larger deviation from the average over three points of up to 10–25%. These data show that the applied analysis technique adequately reflects the composition of the initial silicate melt entrapped in the inclusions.

This difference in color makes it easier to identify S-rich melt inclusions. Many of these are associated with sulfide globules and/or the presence of crystalline anhydrite. The main population of MI from the 1941 Tolbachik eruption contains <4000 ppm S, with a mode of ~2500 ppm, and a relatively normal statistical distribution (Figure 3). Based on limited data, we can infer that the S-rich MI may have a mode of ~8000 ppm.

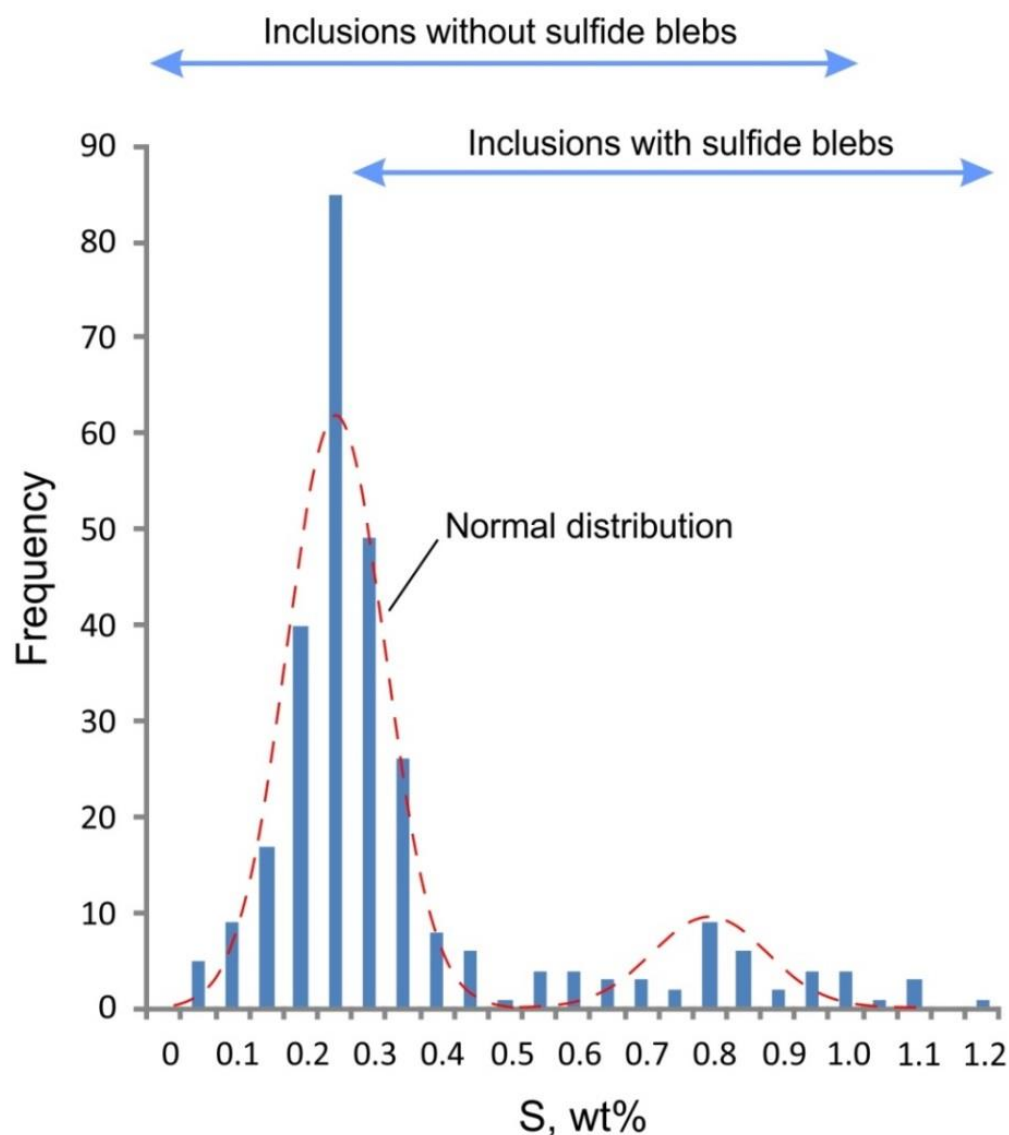


Figure 3. Histogram displaying the distribution of sulfur concentrations in MI from the 1941 Tolbachik eruption; data is the same as for the diagram shown in Figure 2.

3.3. Isotopic Composition of Sulfur

Along with volatile components, the isotopic composition of sulfur in 35 melt inclusions was measured by SIMS (Table 1, Figure 4). The $\delta^{34}\text{S}$ values range from 4.69 ± 2.03 ‰ (2σ), with a mean almost identical to the global average for island-arc rocks ($\delta^{34}\text{S} = +4.5$ ‰, Figure 3) and the sulfur isotopic compositions of the eruptive gases from the 2013 Tolbachik eruption ($\delta^{34}\text{S} = +4.5$, our data). No significant correlations between $\delta^{34}\text{S}$ and total S, or any other element or volatile component were observed. According to Gurenko, A.A. [23], sulfur in MI from scoria does not form significant correlations with either volatile elements or rock-forming oxides, which is in agreement with our observations.

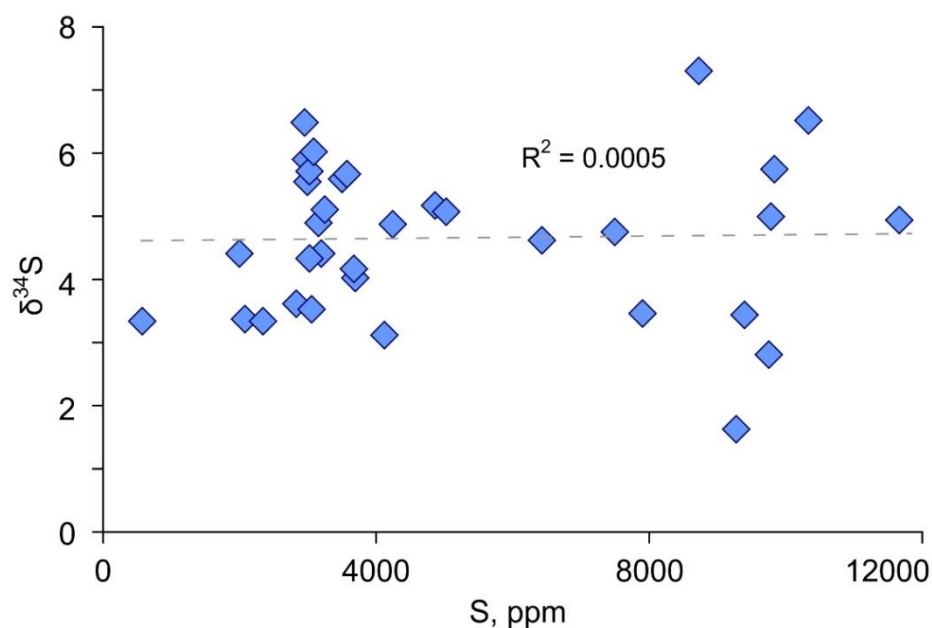


Figure 4. Variation diagram $\delta^{34}\text{S}$ vs. S content, ppm. Zero correlation is visible for the concentration range of sulfur spanning orders of magnitude.

3.4. High Sulfur, Magmatic Sulfides, and Anhydrite

Most inclusions with anomalously high sulfur (≥ 4000 ppm) contain magmatic sulfides and anhydrite, however, some may only host transparent glass (Figures 5 and 6). The sulfur concentrations in sulfide-hosting and sulfide-free inclusions overlap each other to a large extent (Figure 3), although the maximum sulfur concentrations (11,700 ppm) are only recorded in sulfide-containing inclusions. Sulfide globules are observed either directly inside a high-sulfur melt inclusion, or within the same olivine crystal but adjacent to the melt inclusions (Figures 1D and 6).

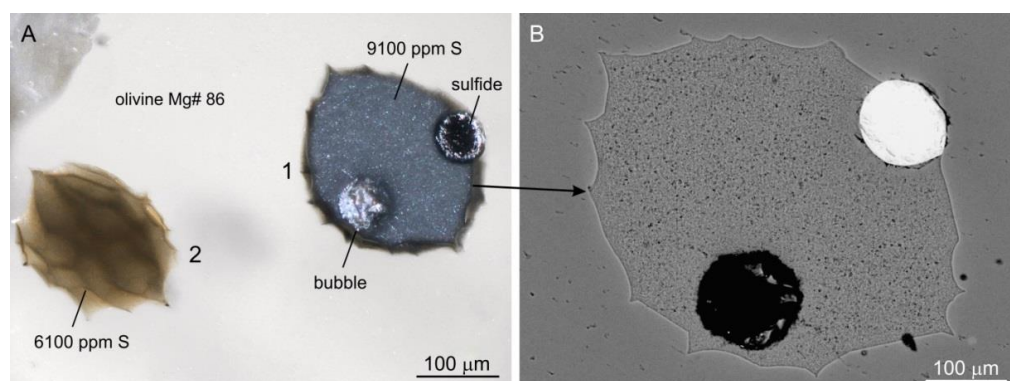


Figure 5. Transmitted light (A) and back-scattered electron (B) images of two melt inclusions within the olivine crystal are shown in Figure 1C which have different degrees of crystallization despite the same quenching rate. A: Inclusion #1 with higher sulfur (9100 ppm) contains a trapped globule of Fe-Ni-Cu sulfide; the adjacent inclusion #2 with a lower sulfur concentration (6100 ppm) is represented by the brown translucent glass and does not contain visible crystals. B: Melt in inclusion #1 occurred within the fine-crystalline, porous aggregate consisting of clinopyroxene, anhydrite, and acid glass.

In addition to sulfide, some melt inclusions host anhydrite. Morphologies of anhydrite aggregates differ from round or deformed globules (up to 20–30 μm ; Figures 7A,B and 8) to μm -sized globules (Figures 7C and 8) and larger crystals (Figure 7D). Small anhydrite globules and crystals likely formed during cooling of the sulfur-rich melt captured in the inclusion. Larger anhydrite globules (e.g., Figures 7A,B and 8) could not form inside the

inclusion during crystallization, as the total mass of the globules significantly exceeds the amount of anhydrite that can dissolve in a given volume of silicate melt. For example, the total mass calculated for two anhydrite globules within the inclusion from Figure 7a is approximately 7% of the volume of the melt, accounting for the volume of globules and the densities of the melt and anhydrite. The deformed globule in Figure 7b occupies ~50% of the residual volume of the inclusion, aside from sulfide and spinel. The large volume of anhydrite, as well as the isometric shape of the globules, indicates the presence of magmatic anhydrite in the basaltic silicate melt at the time of inclusion entrapment by olivine.

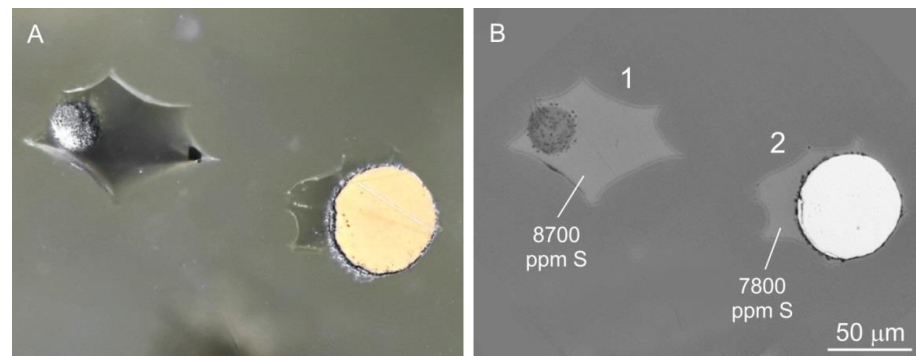


Figure 6. Transmitted light (A) and back-scattered electron (B) images of an adjacent MI in olivine, with and without sulfide globules. Inclusion #2 contains a large Fe-Ni sulfide globule, whereas inclusion #1 only contains a contraction bubble. Both inclusions are represented by transparent glass. Notably, sulfur concentrations in the sulfide-free inclusion #1 reach 8700 ppm, which is higher than those from the sulfide-hosting inclusion #2 (7800 ppm).

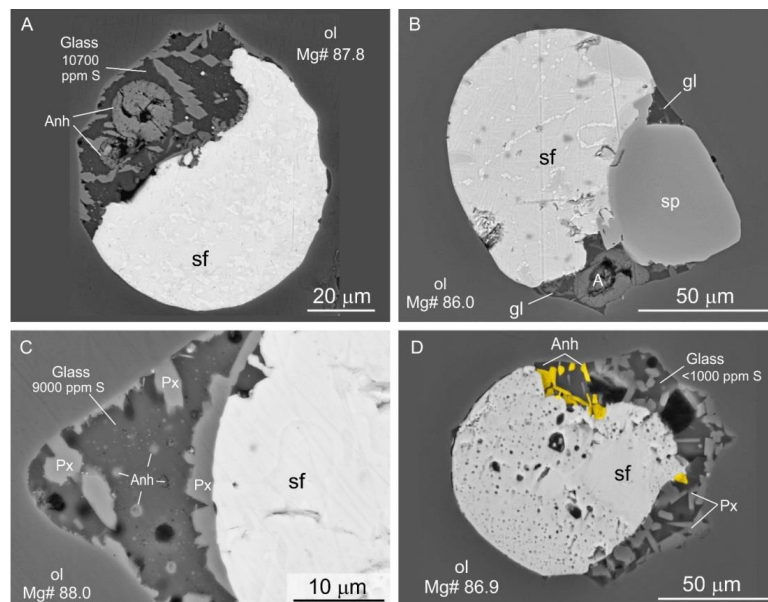


Figure 7. Back-scattered electron images outlining the morphology of anhydrite inclusions in MI. (A) Two spherical globules of anhydrite (~20 μm) enclosed in S-rich glass (~1.07 wt.% S). Dendritic crystals of clinopyroxene are also present. (B) Deformed anhydrite globule located within a pocket of glass between a sulfide globule and spinel crystal. (C) Small globules of anhydrite, presumably precipitated from the cooling silicate melt, are rich in sulfur (~9000 ppm). (D) Anhydrite crystals in residual acid glass (64 wt.% SiO₂) in association with clinopyroxene; glass adjacent to anhydrite crystals is depleted in sulfur and contains no more than 1000 ppm. Anhydrite crystals are highlighted in yellow for clarity. Anh—anhydrite, px—clinopyroxene, sf—sulfide, sp—spinel, ol—olivine, and gl—glass. A, modified from [22].

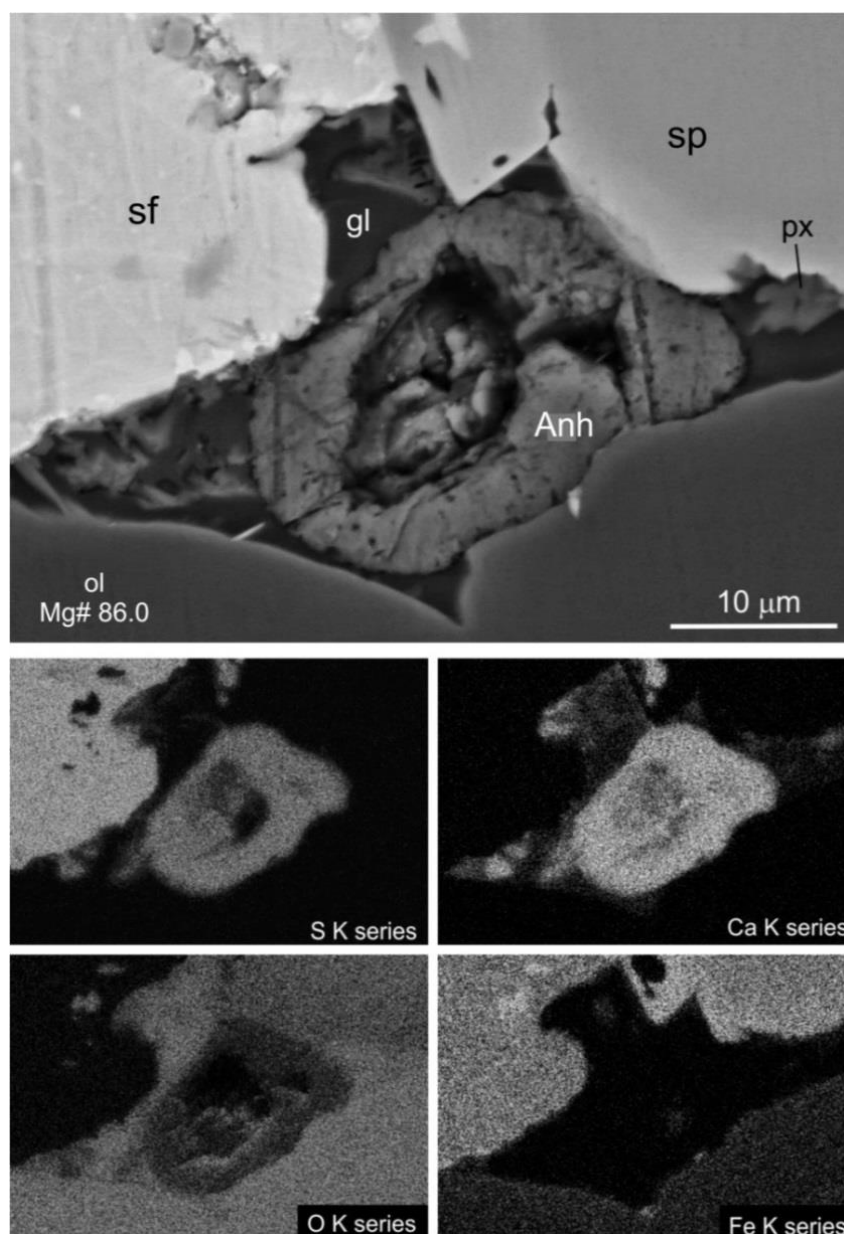


Figure 8. The element map (EDS) of the anhydrite globule is shown in Figure 7B. Anhydrite contains no other cations except calcium. Abbreviations are the same as in Figure 7.

4. Discussion

4.1. Melt Evolution and Comparison with GEOROC Database

Sulfur concentrations in the Tolbachik MI are normally distributed up until 4000 ppm, whereas the lower tail of distribution extends into a higher concentration range approaching 12,000 ppm (Figure 3). In contrast, the distribution of sulfur concentrations from island arc melt inclusions worldwide (GEOROC database) is very close to exponential across the range of 0–7000 ppm (Figure 9). This exponential increase in low sulfur concentrations is likely attributed to melt degassing prior to magma entrapment [3] and does not reflect the initial sulfur content in magmas. Therefore, we can tentatively suggest that the absence of S-poor MI from the Tolbachik 1941 eruption (e.g., Figure 3) indicates that degassing had a relatively weak effect on sulfur concentration in our samples.

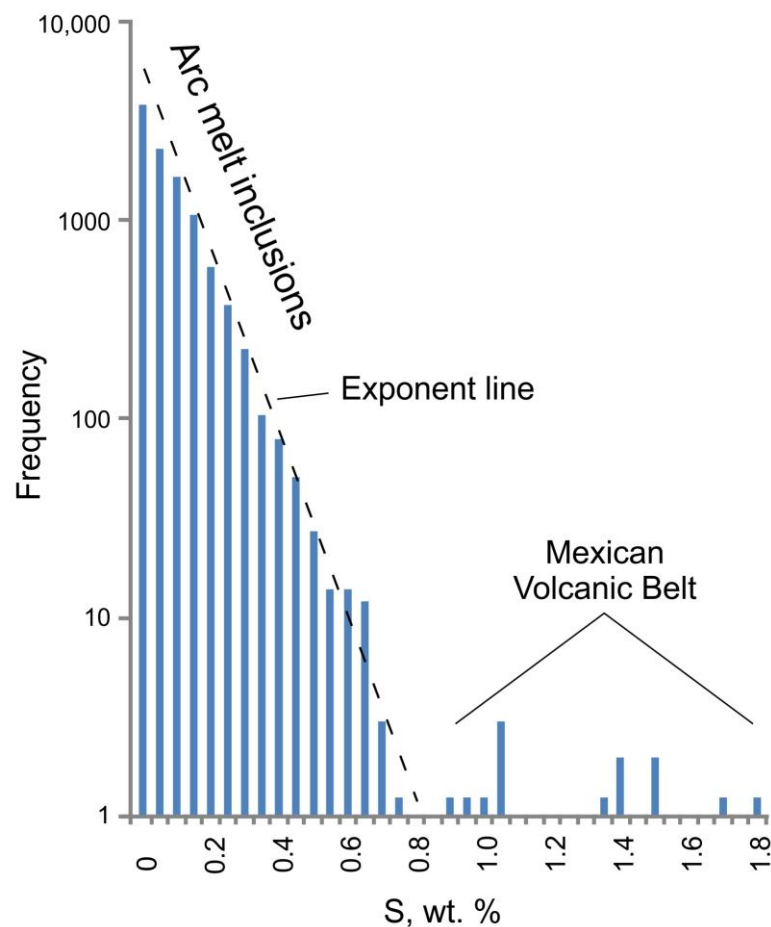


Figure 9. Histogram showing the statistical distribution of sulfur concentrations in melt inclusions from island-arc volcanoes worldwide (without new data on Tolbachik). There is an exponential increase in low S concentrations, aside from alkaline rocks of the Western Mexican Volcanic Belt [15].

Previous studies have used the incompatible nature of K and S during melt evolution as geochemical tracers of magmatic processes [14]. These authors argue that low S/K₂O ratios in MI are the result of degassing. However, these elements may behave differently in certain environments. Sulfur is incompatible in the absence of sulfide or sulfate immiscibility and magma degassing [14], while potassium also remains in the melt at high degrees of evolution, at least until K-dominant phases begin to precipitate (e.g., amphibole, mica, and K-feldspar). Concentrations of both elements in the melt increase with lower degrees of partial melting of mantle peridotite. An important control of sulfur solubility is f_{O_2} in a silicate melt. In the case of flux mantle melting in the presence of oxidized fluids (QFM + 1.7 . . . 2), sulfides contained in the mantle are completely exhausted and partitioned to the melt even at low degrees of partial melting (6–11%, Jugo [3]). During melt degassing, sulfur exsolves into the fluid, whereas potassium remains in the melt. Therefore, the decoupling of sulfur with stable potassium in the melt may occur due to the assimilation of crustal rocks containing abundant sulfates (e.g., hydrothermally altered rocks rich in gypsum, anhydrite, and pyrite).

The variation diagram for K₂O vs. S (Figure 10) demonstrates that most island-arc melt inclusions have a maximum of 3000–4000 ppm S, which corresponds to a range of 0.8–1.2 wt.% K₂O. With an increase in K₂O, sulfur progressively decreases, and at ≥ 5 wt.% K₂O, sulfur concentrations rarely exceed 1000 ppm. The exceptions are high-K rocks from the Mexican Volcanic Belt (MVB), where high concentrations of alkalis and volatiles are associated with local rifting superimposed atop the subduction zone [15,16]. The maximum sulfur concentrations in melt inclusions from the MVB approaches 2 wt.%. However, some

of these inclusions can be classified as low-potassium (0.8–1.2 wt.% K_2O) and contain normal sulfur contents.

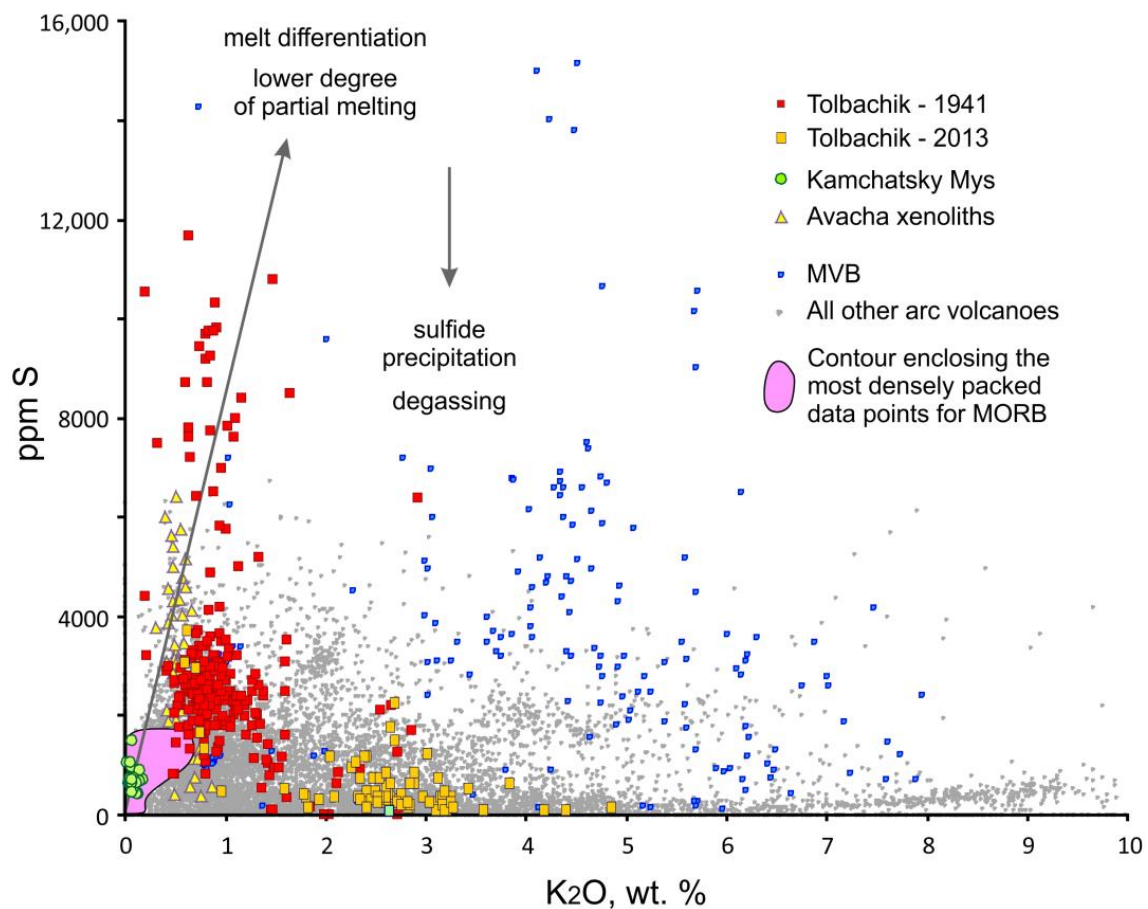


Figure 10. Variation diagram for K_2O (wt.%) vs. S (ppm) for MI from arc volcanoes here and worldwide (sourced from the GEOROC database).

Melt inclusions of the 1941 Tolbachik eruption (magnesian basalt) cluster within the ranges of 0.5–1.5 wt.% K_2O and 1000–3800 ppm S. These may also expand and include high sulfur concentrations, up to ~1.2 wt.% (11,700 ppm S) at the same K_2O . For comparison, data from the 2013 Tolbachik eruption (high-alumina basaltic trachyandesites) are also included. Inclusions from basaltic trachyandesites are depleted in sulfur and enriched in potassium relative to those from magnesian basalts and lie approximately in the center of the geochemical field for all island arc volcanoes (Figure 10).

Data of olivine melt inclusions from plagioclase picrites from Kamchatsky Mys Peninsula (Eastern Kamchatka) are also included in Figure 10 and have low sulfur and K_2O but high S/ K_2O ratios, a characteristic feature of MORB-like melts [29]. These olivine-phyric rocks were found in serpentinite melange around the Mt. Soldatskaya peridotite massif and are interpreted as “the earliest expression of the interaction of the Hawaiian ‘plume’ and paleo-spreading center” [30]. Although MORB melts and the subduction-related Tolbachik magmas are fundamentally different in terms of trace element compositions, they have comparably high S/ K_2O ratios up to 1–1.5 (Figure 11). In other subduction-related melts, such high S/ K_2O ratios are extremely rare for K-poor MI. However, concentrations of other elements are so drastically different in MI from Kamchatsky Mys picrites [29] and Tolbachik [31,32] that it precludes the possibility of any similarity in their melt evolution.

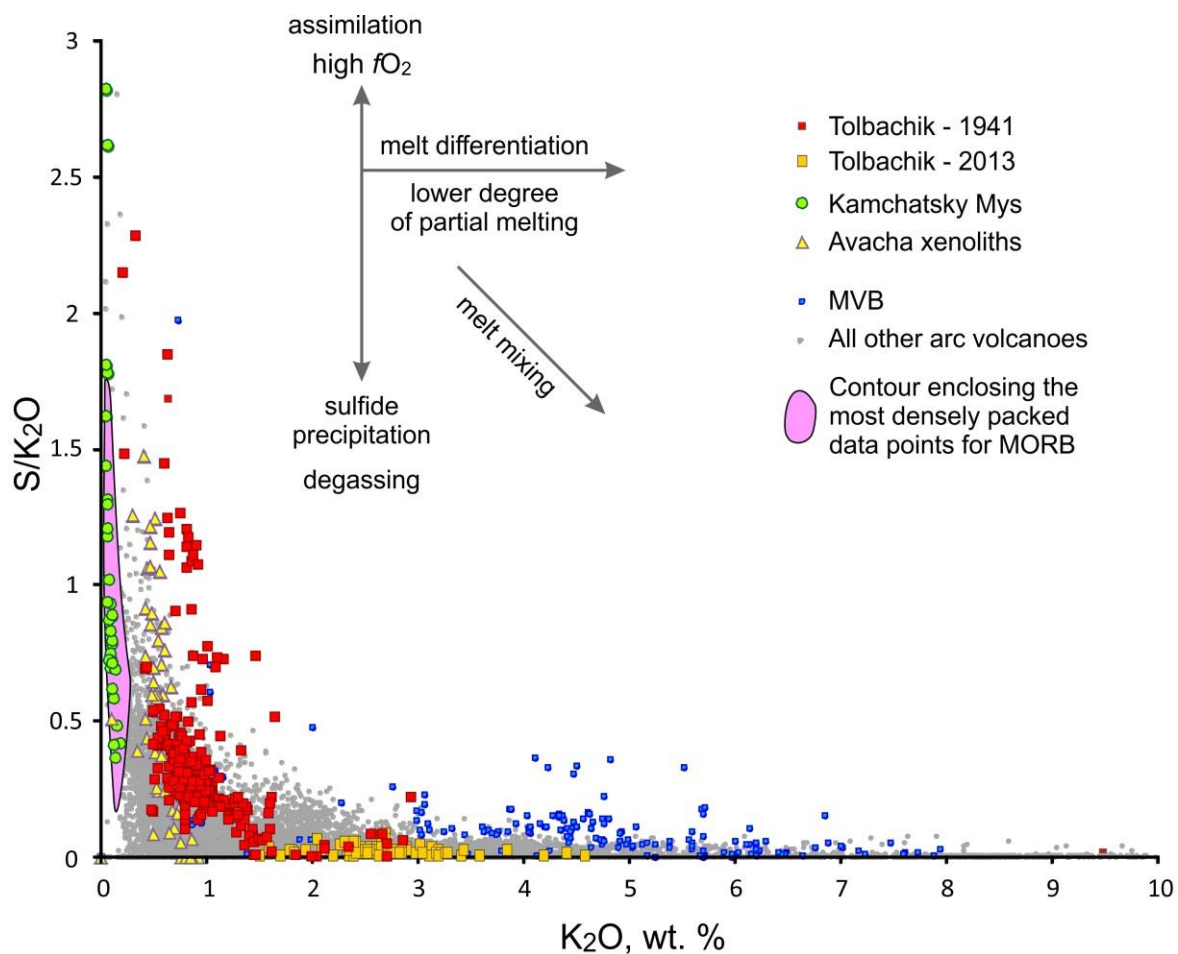


Figure 11. Variation diagram for K_2O (wt.%) vs. S/K_2O for MI from arc volcanoes here and worldwide (sourced from the GEOROC database).

Melt inclusions (~ 60 wt.% SiO_2) in spinels from mantle xenoliths of the Avacha volcano, which were interpreted as entrapped slab melt [33], are also included in Figures 10 and 11. Sulfur concentrations reach 6400 ppm (with $K_2O \sim 0.5$ wt.%), which exceeds almost all island-arc inclusions, except for the MVB volcanoes. Although these sulfur concentrations are high, they are still 1.5–2 times lower than the highest recorded in the Tolbachik MI. Possible processes that may account for anomalously high S concentrations in primary magmas could be interaction with a S-rich slab melt (e.g., 6400 ppm S [33]) and S-rich mantle peridotite (up to 0.5–1% vol.% of base-metal sulfides in pyroxenites or highly metasomatized peridotites, which translates to 2200–5500 ppm S e.g., [34,35]), or when S-rich slab fluid interacts with a conventional depleted MORB-like peridotite mantle (~ 200 ppm S [32]). Both scenarios require further investigation for the Tolbachik magmas. However, Figure 11 demonstrates that both high-sulfur melts and melts with high S/K_2O ratios are present in the subduction zone beneath Kamchatka.

4.2. Anhydrite in Basaltic Melts and Sulfur Saturation

The simultaneous presence of sulfide globules and anhydrite in MI from Tolbachik is intriguing and requires further clarification. Anhydrite rarely occurs in intermediate to felsic volcanic rocks, as well as in basic to felsic intrusive rocks [36–39], and has not been previously reported in basalts or melt inclusions from basalts. Sulfide (pyrrhotite) and anhydrite in natural systems can occur together (e.g., Table 1 in Parat et al. [38] and references therein) if melt fO_2 is in the range where both S^{6+} and S^{2-} may coexist [1,3,4,40]. Published XANES measurements of sulfur speciation in basaltic glasses define a narrow interval for the change from $S^{6+}/\Sigma S = 0.1$ to $S^{6+}/\Sigma S = 0.9$ at QFM + 1.05 ± 0.48 [40]

(Figure 12). Such f_{O_2} values correspond to the measured value for the Tolbachik melt (QFM +1.1 . . . +1.37 [22]) according to the olivine-orthopyroxene-spinel oxygen geobarometer [41]. It is clear from Figure 12 that sufficiently high sulfur, even under moderately oxidizing conditions (\sim QFM +1.1 . . . 1.4), can lead to silicate-sulfide liquid immiscibility. The presence of anhydrite in MI from Tolbachik basalt indicates a high content of S^{6+} (\sim 1–1.2 wt.%) in the silicate melt and accounts for the high total sulfur [40,42,43].

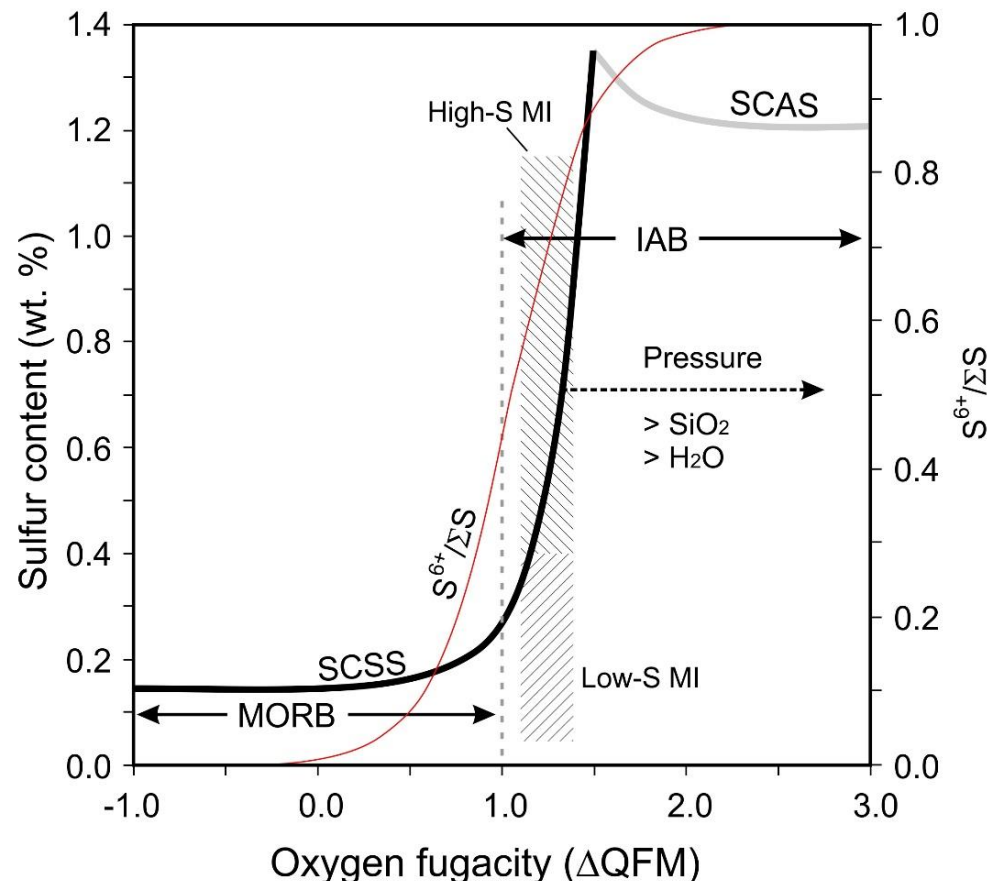


Figure 12. Saturation concentrations of sulfur in silicate melt over sulfide and anhydrite, depending on oxygen fugacity. The section of the sulfide saturation curve (SCSS, sulfur content at sulfide saturation) corresponds to $f_{O_2} < \text{QFM} + 1.5$. For more oxidized melts, the maximum sulfur concentration (SCAS, sulfur content at anhydrite saturation) is determined by the crystallization of magmatic anhydrite from the melt. The maximum possible sulfur concentration in the melt corresponds to the value $f_{O_2} = \text{QFM} + 1.5$. At this value, the SCSS and SCAS curves intersect. The f_{O_2} and sulfur contents for Tolbachik melt inclusions (high-S MI and low-S MI) are shown by hatching. The sulfur speciation curve $S^{6+}/\Sigma S$ vs. f_{O_2} is also shown. Modified from [40].

Strictly speaking, the simultaneous existence of sulfide globules and anhydrite is possible only at the point of intersection of the SCSS and SCAS curves. In Figure 12, this corresponds to $f_{O_2} = \text{QFM} + 1.5$. At any other f_{O_2} value, either sulfide globules or anhydrite should be present in the equilibrium melt. It is unlikely that this condition is so precisely satisfied for the Tolbachik melt. It is much more probable that anhydrite is a secondary phase and formed as a result of local oxidation of sulfide globules scattered in the melt. Large anhydrite spherules up to 20 μm in size (Figures 7A,B and 8) could be of such origin and were captured in inclusions simultaneously with sulfides. Smaller anhydrite globules and crystals (Figure 7C,D) could form directly inside the inclusions during post-entrapment oxidation of the latter.

In the Tolbachik magmas, the relatively high redox potential of the silicate melt likely contributed to the retention of sulfur in the melt. The exsolution of sulfur into a fluid phase

depends on the equilibrium partitioning between fluid and melt. The partition coefficient of sulfur between melt and aqueous fluid crucially depends on fO_2 and has its minimum above NNO + 0.5 (~QFM + 1.2), e.g., [13]. Furthermore, the partition coefficient of sulfur between depolymerized basaltic melts and fluid can be very low, thus contributing to a high concentration of sulfur [44]. Even if anhydrite has already crystallized from the melt in the form of a separate phase, it will be retained in the melt due to the fact that anhydrite has a similar density to basaltic melt at moderate pressures (SG ~ 2.95–3.0 vs. 2.8–3.2 at 2.0 GPa, Bajgain et al. [45]) and, therefore, is not subject to gravitational differentiation, unlike sulfide melt (SG ~ 4.5–5.0). Maria, A.H. and Luhr, J.F. [15] also noted high fO_2 values (several log units above the Ni-NiO redox buffer) for MVB alkaline rocks containing high sulfur.

4.3. Hypotheses for the Origin of High Sulfur in the Tolbachik Melt

Despite extensive research on igneous rocks, melt inclusions, and sulfides of the Tolbachik volcano [22,23,28,31,46–48], precise explanations or data on the origin of the high sulfur anomaly are not yet available. The presence of sulfides or anhydrite in MI does not reveal the origin of sulfur. A distinctive feature of high sulfur rocks of the 1941 Tolbachik eruption is the difference in sulfur concentrations between melt inclusions; only 2% contain S > 4000 ppm, and less than 0.6% contain sulfide globules.

Kamenetsky et al. [22] briefly discuss potential sources of high sulfur for the Tolbachik volcano. These include (#1) the assimilation of sulfur-rich crustal rocks; (#2) the contamination of the melt by volcanic or hydrothermally altered sulfur-rich rocks that may have previously formed around magma conduits, and (#3) the assimilation of a sulfide deposit, possibly magmatic or hydrothermal. All these hypotheses are either incompatible with the chemical and isotopic compositions of the Tolbachik volcanic rocks (hypothesis #1) or are speculative (hypotheses #2 and #3). For example, Gurenko, A.A. [23], and references therein, as well as several earlier works, e.g. [31,49,50], used chemical and radiogenic isotope data to show that no significant assimilation of isotopically contrasting crustal material of the Kamchatka subcontinental crust occurred for Tolbachik magmas. Furthermore, crustal assimilation is not supported by the sulfur isotopes in MI here which is consistently $\delta^{34}S = +4.5$ (e.g., Figure 4).

Another suggested source was secondary magma recharge with previously exsolved S-rich fluid during magma convection [22]. This is also speculative and would involve magma convecting in a chamber that is able to entrain S-rich fluid pockets previously accumulated in the upper part of the chamber, e.g., [51]. None of the suggested hypotheses adequately explain the S-rich MI observed from Tolbachik and their absence from other arc volcanoes with calc-alkaline rocks. Therefore, Kamenetsky et al. [11] concluded that these anomalous S concentrations and textures in MI may simply be a rare phenomenon that has not been recognized in volcanoes elsewhere. This may be the most plausible explanation and is also supported by data from MI measuring up to 10,800 ppm [22,28] in MI from the scoria of the 1941 Tolbachik eruption.

A fundamentally different origin for high sulfur in melt inclusions has been recently suggested by Venugopal et al. [19] which involves the formation of shrinkage bubbles. Melt inclusions have greater thermal expansion rates (2.5–3 times higher) than the host mineral (olivine) e.g., [52,53]. Upon the quenching of the inclusion, the volume of the rapidly cooling melt becomes less than the volume of the cavity in olivine, leading to the formation of a gas bubble. The pressure in such a bubble can be significantly lower than the external pressure (e.g., contraction pressure drop, [27,54,55], and references therein) and volatile components, primarily CO_2 , but also water and volatile sulfur compounds, can exsolve into the bubble. It was shown in Wallace et al. [55] and Venugopal et al. [19] that approximately 85% of CO_2 and 84% of S, can be enclosed in such shrinkage bubbles. If we accept the point of view of Venugopal et al. [19], then we can assume that high sulfur concentrations in the majority of the previous MI studies were not measured simply because most of the sulfur in the inclusions fractionated into the shrinkage bubble, whereas at Tolbachik

such fractionation was weakened. The presence of high-sulfur MI at Tolbachik can thus be explained by higher fO_2 in the melt. This is supported by the presence of dark brown (e.g., oxidized) glass and anhydrite within the S-rich MI (e.g., Figure 5). In such an oxidized silicate melt, sulfur experiences only a little fractionation into a shrinkage bubble due to a lower partition coefficient between fluid and melt, characteristic of silicate melts with higher oxygen fugacity [13] (hypothesis # 6). Therefore, our study indicates that significant exsolution of sulfur to the shrinkage bubbles (e.g., 84% [19]) does not always occur.

A further explanation (hypothesis # 7) for the locally S-rich MI from Tolbachik is that a portion of the melt interacted with an anomalously oxidized slab fluid. This should have led to greater sulfide exhaustion from mantle peridotite and simultaneous enrichment of primary melt by Cu and PGE [3,56]. Indeed, the Tolbachik-1941 lavas are slightly enriched in Cu, Pd, and Pt (up to 234 ppm Cu, 7.8 ppb Pd, and 6.1 ppb Pt) relative to magnesian basalts, e.g., [57]. More importantly, the sulfide globules from Tolbachik [22,28] also contain concentrations of Pd and Pt among the highest ever measured in sulfide globules (up to 299 ppm Pd and 115 ppm Pt, Zelenski et al. [58]).

5. Conclusions

Anomalously high sulfur concentrations in the range of 4000–11700 ppm were measured in naturally quenched melt inclusions in olivine from the 1941 Tolbachik eruption, Kamchatka. Such concentrations are the highest ever recorded in MI from primitive arc basalts. These high values account for only 2% of the analyzed inclusions, whereas the majority of inclusions contain 2500 ± 1500 ppm. Sulfur correlates well with Cl in most of the S-poor inclusions and follows a degassing trend. Measured $\delta^{34}S$ values are close to the global average for island-arc rocks and arc volcanic gases ($\delta^{34}S = +4.5$), but do not correlate with sulfur concentrations. Many S-rich melt inclusions contain magmatic sulfide globules and anhydrite enclosed within a brown, oxidized glass. The simultaneous presence of sulfide and anhydrite in MI indicates a narrow range of $fO_2 = QFM + 1.1 \pm 0.5$ for the Tolbachik melt, which is equal to fO_2 previously determined for the same melt using a spinel-olivine-orthopyroxene oxybarometer.

The drastic difference in S concentrations and S/K₂O ratios between the sulfur-rich and sulfur-poor (normal) populations of melt inclusions requires further investigation. Possible explanations include assimilation of crustal material or hydrothermally altered rocks, sulfide mineralization, or S-rich magmatic fluids. We speculate that some brown (oxidized) S-rich melt inclusions, which contain sulfide globules enriched in Cu, Pd, and Pt, are associated with complete exhaustion of mantle sulfides during the melt interaction with locally oxidized slab fluid. Alternatively, the systematic underestimation of S in all previously studied melt inclusions due to significant fractionation into shrinkage bubbles could also be considered.

Supplementary Materials: The following are available online at <https://www.mdpi.com/article/10.3390/min12010037/s1>, Figure S1: Satellite image (Google Earth) of the 1941 cone on Tolbachik, Kamchatka, and the sampling field; Figure S2: The 1941 scoria cone and the adjacent scoria field. Photo by M. Zelenski; Figure S3: Large melt inclusion in olivine that underwent slow cooling. The 1941 Tolbachik eruption, lava flow. The sizes of daughter crystals are 20–30% of the diameter of the entire inclusion. The inclusion contains clinopyroxene, amphibole, magnetite, acid glass and several vapor bubbles.; Figure S4: A cluster of normal (non-oxidized) melt inclusions with light brown glass and a sulfur content of about 3000 ppm S; Figure S5: An olivine crystal with a sulfide swarm and melt inclusions filled with dark brown glass. Four sulfide globules are exposed; more globules are enclosed in olivine. The 1941 Tolbachik eruption; Figure S6: An olivine crystal with a swarm of sulfide globules and melt inclusions filled with dark brown glass. One sulfide globule is exposed. Numerous inclusions of brown chromite are also present. The 1941 Tolbachik eruption. Table S1: Bulk composition of scoria from the 1941 eruption, Tolbachik volcano, Kamchatka; Table S2: Compositions of silicate melt inclusions in olivine, and basaltic glass, the 1941 eruption, Tolbachik volcano, Kamchatka.

Author Contributions: Conceptualization, M.Z., V.S.K. and N.N.; methodology, M.Z.; investigation, M.Z., V.S.K. and N.N.; resources, M.Z., and V.S.K.; writing—original draft preparation, M.Z., V.S.K. and N.N.; writing—review and editing, M.Z., V.S.K., N.N. and A.K.-C.; project administration, M.Z. and V.S.K. All authors have read and agreed to the published version of the manuscript.

Funding: This research was funded by RUSSIAN SCIENCE FOUNDATION, grant number 21-17-00122.

Data Availability Statement: Not applicable.

Acknowledgments: We thank A. Gurenko for measurements of volatile content and sulfur isotopic composition in melt inclusions performed on SIMS, N. Nekrasov for his support in EDS measurements, and N. Kononkova for the EMPA studies. We are grateful for three reviewers, whose comments helped us to improve the manuscript.

Conflicts of Interest: The authors declare no conflict of interest.

References

1. Wilke, M.; Klimm, K.; Kohn, S.C. Spectroscopic studies on sulfur speciation in synthetic and natural glasses. *Rev. Mineral. Geochem.* **2011**, *73*, 41–78. [[CrossRef](#)]
2. Baker, D.R.; Moretti, R. Modeling the solubility of sulfur in magmas: A 50-year old geochemical challenge. *Rev. Mineral. Geochem.* **2011**, *73*, 167–213. [[CrossRef](#)]
3. Jugo, P.J. Sulfur content at sulfide saturation in oxidized magmas. *Geology* **2009**, *37*, 415–418. [[CrossRef](#)]
4. Jugo, P.J.; Luth, R.W.; Richards, J.P. An experimental study of the sulfur content in basaltic melts saturated with immiscible sulfide or sulfate liquids at 1300 °C and 1.0 GPa. *J. Petrol.* **2005**, *46*, 783–798. [[CrossRef](#)]
5. Zajacz, Z.; Tsay, A. An accurate model to predict sulfur concentration at anhydrite saturation in silicate melts. *Geochim. Cosmochim. Acta* **2019**, *261*, 288–304. [[CrossRef](#)]
6. Mavrogenes, J.A.; O'Neill, H.S.C. The relative effects of pressure, temperature and oxygen fugacity on the solubility of sulfide in mafic magmas. *Geochim. Cosmochim. Acta* **1999**, *63*, 1173–1180. [[CrossRef](#)]
7. Li, C.S.; Ripley, E.M. Sulfur contents at sulfide-liquid or anhydrite saturation in silicate melts: Empirical equations and example applications. *Econ. Geol.* **2009**, *104*, 405–412. [[CrossRef](#)]
8. Ariskin, A.A.; Danyushevsky, L.V.; Bychkov, K.A.; McNeill, A.W.; Barmina, G.S.; Nikolaev, G.S. Modeling solubility of Fe-Ni sulfides in basaltic magmas: The effect of nickel. *Econ. Geol.* **2013**, *108*, 1983–2003. [[CrossRef](#)]
9. Fortin, M.-A.; Riddle, J.; Desjardins-Langlais, Y.; Baker, D.R. The effect of water on the sulfur concentration at sulfide saturation (SCSS) in natural melts. *Geochim. Cosmochim. Acta* **2015**, *160*, 100–116. [[CrossRef](#)]
10. Moretti, R.; Baker, D.R. Modeling the interplay of f_{O_2} and f_{S_2} along the FeS-silicate melt equilibrium. *Chem. Geol.* **2008**, *256*, 286–298. [[CrossRef](#)]
11. Matjuschkin, V.; Blundy, J.D.; Brooker, R.A. The effect of pressure on sulphur speciation in mid-to deep-crustal arc magmas and implications for the formation of porphyry copper deposits. *Contrib. Mineral. Petrol.* **2016**, *171*, 66. [[CrossRef](#)]
12. Witham, F.; Blundy, J.; Kohn, S.C.; Lesne, P.; Dixon, J.; Churakov, S.V.; Botcharnikov, R. SolEx: A model for mixed COHSCI-volatile solubilities and exsolved gas compositions in basalt. *Comput. Geosci.* **2012**, *45*, 87–97. [[CrossRef](#)]
13. Zajacz, Z.; Candela, P.A.; Piccoli, P.M.; Sanchez-Valle, C. The partitioning of sulfur and chlorine between andesite melts and magmatic volatiles and the exchange coefficients of major cations. *Geochim. Cosmochim. Acta* **2012**, *89*, 81–101. [[CrossRef](#)]
14. Wallace, P.J.; Edmonds, M. The sulfur budget in magmas: Evidence from melt inclusions, submarine glasses, and volcanic gas emissions. *Rev. Mineral. Geochem.* **2011**, *73*, 215–246. [[CrossRef](#)]
15. Maria, A.H.; Luhr, J.F. Lamprophyres, basanites, and basalts of the Western Mexican Volcanic Belt: Volatile contents and a Vein-wallrock melting relationship. *J. Petrol.* **2008**, *49*, 2123–2156. [[CrossRef](#)]
16. Vigouroux, N.; Wallace, P.J.; Kent, A.J.R. Volatiles in high-K magmas from the Western trans-Mexican volcanic belt: Evidence for fluid fluxing and extreme enrichment of the mantle wedge by subduction processes. *J. Petrol.* **2008**, *49*, 1589–1618. [[CrossRef](#)]
17. Cervantes, P.; Wallace, P.J. Role of H₂O in subduction-zone magmatism: New insights from melt inclusions in high-Mg basalts from central Mexico. *Geology* **2003**, *31*, 235–238. [[CrossRef](#)]
18. Narvaez, D.F.; Rose-Koga, E.F.; Samaniego, P.; Koga, K.T.; Hidalgo, S. Constraining magma sources using primitive olivine-hosted melt inclusions from Puñalica and Sangay volcanoes (Ecuador). *Contrib. Mineral. Petrol.* **2018**, *173*, 80. [[CrossRef](#)]
19. Venugopal, S.; Schiavi, F.; Moune, S.; Bolfan-Casanova, N.; Druitt, T.; Williams-Jones, G. Melt inclusion vapour bubbles: The hidden reservoir for major and volatile elements. *Sci. Rep.* **2020**, *10*, 9034. [[CrossRef](#)] [[PubMed](#)]
20. Hauri, E.; Wang, J.; Dixon, J.E.; King, P.L.; Mandeville, C.; Newman, S. SIMS analysis of volatiles in silicate glasses: 1. Calibration, matrix effects and comparisons with FTIR. *Chem. Geol.* **2002**, *183*, 99–114. [[CrossRef](#)]
21. Gurenko, A.A.; Kamenetsky, V.S.; Kerr, A. Oxygen isotopes and volatile contents of the Gorgona komatiites, Colombia: A confirmation of the deep mantle origin of H₂O. *Earth Planet. Sci. Lett.* **2016**, *454*, 154–165. [[CrossRef](#)]

22. Kamenetsky, V.S.; Zelenski, M.; Gurenko, A.; Portnyagin, M.; Ehrig, K.; Kamenetsky, M.; Churikova, T.; Feig, S. Silicate-sulfide liquid immiscibility in modern arc basalt (Tolbachik volcano, Kamchatka): Part II. Composition, liquidus assemblage and fractionation of the silicate melt. *Chem. Geol.* **2017**, *471*, 92–110. [[CrossRef](#)]
23. Gurenko, A.A. Origin of sulphur in relation to silicate-sulphide immiscibility in Tolbachik primitive arc magma (Kamchatka, Russia): Insights from sulphur and boron isotopes. *Chem. Geol.* **2021**, *576*, 120244. [[CrossRef](#)]
24. Davis, M.J.; Ihinger, P.D.; Lasaga, A.C. Influence of water on nucleation kinetics in silicate melt. *J. Non Cryst. Solids* **1997**, *219*, 62–69. [[CrossRef](#)]
25. Gonzalez-Oliver, C.J.R.; Johnson, P.S.; James, P.F. Influence of water content on the rates of crystal nucleation and growth in lithia-silica and soda-lime-silica glasses. *J. Mater. Sci.* **1979**, *14*, 1159–1169. [[CrossRef](#)]
26. Potapov, O.V.; Fokin, V.M.; Filipovich, V.N. Nucleation and crystal growth in water containing soda–lime–silica glasses. *J. Non Cryst. Solids* **1999**, *247*, 74–78. [[CrossRef](#)]
27. Gavrilenko, M.; Krawczynski, M.; Ruprecht, P.; Li, W.; Catalano, J.G. The quench control of water estimates in convergent margin magmas. *Am. Mineral.* **2019**, *104*, 936–948. [[CrossRef](#)]
28. Zelenski, M.; Kamenetsky, V.S.; Mavrogenes, J.A.; Gurenko, A.A.; Danyushevsky, L.V. Silicate-sulfide liquid immiscibility in modern arc basalt (Tolbachik volcano, Kamchatka): Part I. Occurrence and compositions of sulfide melts. *Chem. Geol.* **2018**, *478*, 102–111. [[CrossRef](#)]
29. Korneeva, A.A.; Nekrylov, N.; Kamenetsky, V.; Portnyagin, M.; Krashennnikov, S.P.; Savelyev, D.P.; Abersteiner, A.; Kamenetsky, M.; Zelenski, M.E.; Shcherbakov, V. Composition, crystallization conditions and genesis of sulfide-saturated parental melts of olivine-phyric rocks from Kamchatsky Mys (Kamchatka, Russia). *Lithos* **2020**, *370–371*, 105657. [[CrossRef](#)]
30. Savelyev, D.P. Plagioclase picrites in the Kamchatsky Mys Peninsula, Eastern Kamchatka. *J. Volcanol. Seismol.* **2014**, *8*, 239–249. [[CrossRef](#)]
31. Portnyagin, M.; Duggen, S.; Hauff, F.; Mironov, N.; Bindeman, I.; Thirlwall, M.; Hoernle, K. Geochemistry of the late Holocene rocks from the Tolbachik volcanic field, Kamchatka: Quantitative modelling of subduction-related open magmatic systems. *J. Volcanol. Geotherm. Res.* **2015**, *307*, 133–155. [[CrossRef](#)]
32. Mironov, N.; Portnyagin, M. Coupling of redox conditions of mantle melting and copper and sulfur contents in primary Magmas of the Tolbachinsky Dol (Kamchatka) and Juan de Fuca Ridge (Pacific Ocean). *Petrology* **2018**, *26*, 145–166. [[CrossRef](#)]
33. Ionov, D.A.; Bénard, A.; Plechov, P.Y. Melt evolution in subarc mantle: Evidence from heating experiments on spinel-hosted melt inclusions in peridotite xenoliths from the andesitic Avacha volcano (Kamchatka, Russia). *Contrib. Mineral. Petrol.* **2011**, *162*, 1159–1174. [[CrossRef](#)]
34. Dromgoole, E.L.; Pasteris, J.D. Interpretation of the Sulfide Assemblages in a Suite of Xenoliths. In *Mantle Metasomatism and Alkaline Magmatism*; Geological Society of America: Boulder, CO, USA, 1987.
35. Lorand, J.-P.; Luguét, A. Chalcophile and siderophile elements in mantle rocks: Trace elements controlled by trace Minerals. *Rev. Mineral. Geochem.* **2016**, *81*, 441–488. [[CrossRef](#)]
36. Baker, L.L.; Rutherford, M.J. Crystallisation of anhydrite-bearing magmas. *Earth Environ. Sci. Trans. R. Soc. Edinb.* **1996**, *87*, 243–250.
37. Luhr, J.F.; Carmichael, I.S.E.; Varekamp, J.C. The 1982 eruptions of El Chichon volcano, Chiapas, Mexico: Mineralogy and petrology of the anhydrite-bearing pumices. *J. Volcanol. Geotherm. Res.* **1984**, *23*, 69–108. [[CrossRef](#)]
38. Parat, F.; Holtz, F.; Streck, M.J. Sulfur-bearing magmatic accessory minerals. *Rev. Mineral. Geochem.* **2011**, *73*, 285–314. [[CrossRef](#)]
39. Pasteris, J.D. Mount Pinatubo volcano and “negative” porphyry copper deposits. *Geology* **1996**, *24*, 1075–1078. [[CrossRef](#)]
40. Jugo, P.J.; Wilke, M.; Botcharnikov, R.E. Sulfur K-edge XANES analysis of natural and synthetic basaltic glasses: Implications for S speciation and S content as function of oxygen fugacity. *Geochim. Cosmochim. Acta* **2010**, *74*, 5926–5938. [[CrossRef](#)]
41. Ballhaus, C.; Berry, R.F.; Green, D.H. High pressure experimental calibration of the olivine-orthopyroxene-spinel oxygen geobarometer: Implications for the oxidation state of the upper mantle. *Contrib. Mineral. Petrol.* **1991**, *107*, 27–40. [[CrossRef](#)]
42. Jugo, P.J.; Luth, R.W.; Richards, J.P. Experimental data on the speciation of sulfur as a function of oxygen fugacity in basaltic melts. *Geochim. Cosmochim. Acta* **2005**, *69*, 497–503. [[CrossRef](#)]
43. Li, C.S.; Ripley, E.M. Empirical equations to predict the sulfur content of mafic magmas at sulfide saturation and applications to magmatic sulfide deposits. *Mineral. Deposita* **2005**, *40*, 218–230. [[CrossRef](#)]
44. Zajacz, Z. The effect of melt composition on the partitioning of oxidized sulfur between silicate melts and magmatic volatiles. *Geochim. Cosmochim. Acta* **2015**, *158*, 223–244. [[CrossRef](#)]
45. Bajgain, S.; Ghosh, D.B.; Karki, B.B. Structure and density of basaltic melts at mantle conditions from first-principles simulations. *Nat. Commun.* **2015**, *6*, 8578. [[CrossRef](#)]
46. Churikova, T.G.; Gordeychik, B.N.; Edwards, B.R.; Ponomareva, V.V.; Zelenin, E.A. The Tolbachik volcanic massif: A review of the petrology, volcanology and eruption history prior to the 2012–2013 eruption. *J. Volcanol. Geotherm. Res.* **2015**, *307*, 3–21. [[CrossRef](#)]
47. Plechov, P.; Blundy, J.; Nekrylov, N.; Melekhova, E.; Shcherbakov, V.; Tikhonova, M.S. Petrology and volatile content of magmas erupted from Tolbachik Volcano, Kamchatka, 2012–2013. *J. Volcanol. Geotherm. Res.* **2015**, *307*, 182–199. [[CrossRef](#)]
48. Volynets, A.O.; Edwards, B.R.; Melnikov, D.; Yakushev, A.; Griboedova, I. Monitoring of the volcanic rock compositions during the 2012–2013 fissure eruption at Tolbachik volcano, Kamchatka. *J. Volcanol. Geotherm. Res.* **2015**, *307*, 120–132. [[CrossRef](#)]

49. Portnyagin, M.; Bindeman, I.; Hoernle, K.; Hauff, F. Geochemistry of Primitive Lavas of the Central Kamchatka Depression: Magma Generation at the Edge of the Pacific Plate. In *Volcanism and Subduction: The Kamchatka Region*; Eichelberger, J., Gordeev, E., Izbekov, P., Kasahara, M., Lees, J., Eds.; Wiley: Hoboken, NJ, USA, 2007; pp. 199–239.
50. Churikova, T.G.; Gordeychik, B.N.; Iwamori, H.; Nakamura, H.; Ishizuka, O.; Nishizawa, T.; Haraguchi, S.; Miyazaki, T.; Vaglarov, B.S. Petrological and geochemical evolution of the Tolbachik volcanic massif, Kamchatka, Russia. *J. Volcanol. Geotherm. Res.* **2015**, *307*, 156–181. [[CrossRef](#)]
51. Allard, P.; Burton, M.; Mure, F. Spectroscopic evidence for a lava fountain driven by previously accumulated magmatic gas. *Nature* **2005**, *433*, 407–410. [[CrossRef](#)]
52. Suzuki, I. Thermal expansion of periclase and olivine, and their anharmonic properties. *J. Phys. Earth* **1975**, *23*, 145–159. [[CrossRef](#)]
53. Fluegel, A.; Earl, D.A.; Varshneya, A.K.; Seward, T.P. Density and thermal expansion calculation of silicate glass melts from 1000 °C to 1400 °C. *Phys. Chem. Glass Eur. J. Glass Sci. Technol. B* **2008**, *49*, 245–257.
54. Zhang, Y. Mechanical and phase equilibria in inclusion-host systems. *Earth Planet. Sci. Lett.* **1998**, *157*, 209–222. [[CrossRef](#)]
55. Wallace, P.J.; Kamenetsky, V.S.; Cervantes, P. Melt inclusion CO₂ contents, pressures of olivine crystallization, and the problem of shrinkage bubbles. *Am. Mineral.* **2015**, *100*, 787–794. [[CrossRef](#)]
56. Mungall, J.E. Roasting the mantle: Slab melting and the genesis of major Au and Au-rich Cu deposits. *Geology* **2002**, *30*, 915–918. [[CrossRef](#)]
57. Kutyrev, A.V.; Zelenski, M.; Nekrylov, N.; Savelyev, D.P.; Kontonikas-Charos, A.; Kamenetsky, V.S. Noble metals in arc basaltic magmas worldwide: A case study of modern and pre-historic lavas of the Tolbachik volcano, Kamchatka. *Front. Earth Sci.* **2021**, *9*, 791465. [[CrossRef](#)]
58. Zelenski, M.; Kamenetsky, V.S.; Mavrogenes, J.A.; Danyushevsky, L.V.; Matveev, D.; Gurenko, A.A. Platinum-group elements and gold in sulfide melts from modern arc basalt (Tolbachik volcano, Kamchatka). *Lithos* **2017**, *290–291*, 172–188. [[CrossRef](#)]